

# Unraveling the inner substructure of new candidate hub-filament system in the HII region G25.4NW

L. K. Dewangan<sup>1\*</sup>

<sup>1</sup>*Physical Research Laboratory, Navrangpura, Ahmedabad - 380 009, India.*

## ABSTRACT

We present multi-scale and multi-wavelength data of the Galactic H II region G25.4-0.14 (hereafter G25.4NW, distance  $\sim 5.7$  kpc). The SHARC-II 350  $\mu\text{m}$  continuum map displays a hub-filament configuration containing five parsec scale filaments and a central compact hub. Through the 5 GHz radio continuum map, four ionized clumps (i.e., Ia–Id) are identified toward the central hub, and are powered by massive OB-stars. The *Herschel* temperature map depicts the warm dust emission (i.e.,  $T_d \sim 23$ –39 K) toward the hub. High resolution Atacama Large Millimeter/submillimeter Array (ALMA) 1.3 mm continuum map (resolution  $\sim 0''.82 \times 0''.58$ ) reveals three cores (c1–c3; mass  $\sim 80$ –130  $M_\odot$ ) toward the ionized clumps Ia, and another one (c4; mass  $\sim 70 M_\odot$ ) toward the ionized clump Ib. A compact near-infrared (NIR) emission feature (extent  $\sim 0.2$  pc) is investigated toward the ionized clump Ia excited by an O8V-type star, and contains at least three embedded K-band stars. In the direction of the ionized clump Ia, the ALMA map also shows an elongated feature (extent  $\sim 0.2$  pc) hosting the cores c1–c3. All these findings together illustrate the existence of a small cluster of massive stars in the central hub. Considering the detection of the hub-filament morphology and the spatial locations of the mm cores, a global non-isotropic collapse (GNIC) scenario appears to be applicable in G25.4NW, which includes the basic ingredients of the global hierarchical collapse and clump-fed accretion models. Overall, the GNIC scenario explains the birth of massive stars in G25.4NW.

**Key words:** dust, extinction – HII regions – ISM: clouds – ISM: individual object (G25.4NW) – stars: formation – stars: pre-main sequence

## 1 INTRODUCTION

Massive OB-type stars ( $M \gtrsim 8 M_\odot$ ), through ultraviolet (UV) radiation, stellar winds, radiation pressure and supernova explosions, have shaped the formation and evolution of galaxies. However, the problem of massive star formation (MSF) is still unsettled (e.g., Zinnecker & Yorke 2007; Tan et al. 2014; Motte et al. 2018; Hirota et al. 2018; Rosen et al. 2020). Concerning MSF, the process of mass accumulation through inflow from larger scales has recently received significant attention (Rosen et al. 2020). In particular, a hub-filament system has been thought as the important observational site, where several parsec-scale filaments intersect the central denser regions (e.g., Myers 2009; Schneider et al. 2012; Motte et al. 2018; Treviño-Morales et al. 2019; Kumar et al. 2020; Dewangan et al. 2020, and references therein). On the basis of the hub-filament system, an evolutionary scheme for MSF (i.e., a global non-isotropic collapse

scenario (GNIC); see Motte et al. 2018; Tigé et al. 2017) is proposed. In this scenario, infrared bright massive protostars grow from low mass stellar embryos, which gain the material through gravitationally-driven inflows from the parental massive dense cores/clumps (MDCs, in a 0.1 pc scale; see Figure 8 in Tigé et al. 2017). These MDCs are firstly developed by a large amount of inflowing gas through filaments. In this relation, one needs to identify the embedded filaments along with the central hub and to explore the inner environments of the central hub hosting massive OB-type stars. In this context, the target of this paper is a prominent Ultra Compact (UC) H II region GPSR5 25.398-0.141 or G25.4-0.14 (hereafter G25.4NW).

Situated at a near-side distance of 5.7 kpc, G25.4NW lies in the inner Galactic molecular ring region, and is excited by at least an O6-type star (Zhu et al. 2011; Ai et al. 2013). The molecular gas toward G25.4NW was studied in a velocity range of [90, 101]  $\text{km s}^{-1}$  (Ai et al. 2013). G25.4NW is associated with a dust continuum source (or clump) JCMT 18354-0649N (hereafter J18354N) (Lester et al. 1985), which is located about  $1'$  north of other dust con-

\* lokeshd@prl.res.in

tinuum source JCMT 18354-0649S (hereafter J18354S) (see Figure 1 in Carolan et al. 2009). It was reported that the clump J18354S has a more compact appearance than the clump J18354N in the SCUBA dust continuum maps at 450 and 850  $\mu\text{m}$  (Wu et al. 2005). Zhu et al. (2011) presented sub-arcsecond resolution H-, K-, and L'-band images toward both the continuum sources, which were observed using the United Kingdom Infrared Telescope (UKIRT) facility. The near-infrared (NIR) nebulosity was seen toward the central part of J18354N, where at least three stars were observed (see Figure 3 in Zhu et al. 2011). However, there are no dust continuum maps with sub-arcsecond resolution reported toward G25.4NW. But, such observations were presented toward the clump J18354S (see Liu et al. (2011) and also Figure D.6 in Zhang et al. (2019)). A green fuzzy object or an extended green object (EGO) has been identified toward J18354S using the *Spitzer* infrared images (see Figure 1 in Carolan et al. 2009), where inflow and outflow motions were investigated (Zhu et al. 2011; Zhang et al. 2019, 2020). In the direction of the EGO buried in the source J18354S, Zhu et al. (2011) identified an embedded source (i.e., IRS1a) in the UKIRT K-band image that was characterized as a massive protostar ( $M \sim 6\text{--}12 M_{\odot}$ ; see Figure 3 in Zhu et al. 2011). It was also suggested that the massive protostar is forming through rapid accretion (Wu et al. 2005; Liu et al. 2011; Zhu et al. 2011; Zhang et al. 2019, 2020). However, the formation process of the massive O-type star in G25.4NW is yet to be explored.

In the literature, there is no study available using the high resolution sub-millimeter (sub-mm) or millimeter (mm) continuum data toward G25.4NW, which can be used to examine the presence of filaments and cores. In this paper, we aim to understand the physical process related to the birth of the O-type star in G25.4NW, which also includes understanding of the mechanism of mass accumulation in MSF. In this context, we employ multi-scale and multi-wavelength data sets of the continuum source JCMT 18354N or G25.4NW, which include the high resolution 5 GHz radio continuum map and the Atacama Large Millimeter/submillimeter Array (ALMA) continuum maps. Furthermore, we revisit several published multi-wavelength data of G25.4NW for exploring its physical environment. In Section 2, we list various observational data sets utilized in this paper. Section 3 presents observational outcomes at different scales and different wavelengths toward G25.4NW. It includes the identification of filaments, ionized clumps, and dust continuum sources toward G25.4NW. In Section 4, we discuss the implications of our observed outcomes. Finally, Section 5 summarizes the major findings.

## 2 DATA SETS

The paper utilizes several observational data sets from available surveys, which are listed in Table 1. The data sets were downloaded toward an area of  $\sim 6.6 \times 4.2$  containing G25.4NW, which is centered at  $l = 25^{\circ}.39$ ;  $b = -0^{\circ}.135$  (Figure 1). In this paper, our study exclusively focuses on the source J18354N or G25.4NW. Hence, we do not discuss the observational results of the well studied source J18354S.

Additionally, we retrieved the ALMA 1.3 mm continuum map (resolution  $\sim 0''.82 \times 0''.58$ , P.A. =  $-69^{\circ}.9$ ,  $1\sigma$

$\sim 0.4$  mJy beam $^{-1}$ ) from the ALMA science archive (project #2017.1.01116.S; PI: Shirley, Yancy). We explored the *Herschel* temperature ( $T_d$ ) map (resolution  $\sim 12''$ ; Molinari et al. 2010b; Marsh et al. 2015, 2017) of G25.4NW. The Bayesian *PPMAP* procedure (Marsh et al. 2015, 2017) was used to build the *Herschel* map. We obtained the processed mid-infrared (MIR) image at 19.7  $\mu\text{m}$  (resolution  $\sim 2''.5$ ) of G25.4NW from the NASA/IPAC infrared science archive (Plan ID: 06.0042; PI: Jonathan Tan), which was observed with the SOFIA Faint Object infraRed CAmera for the SOFIA Telescope (FORCAST; Herter et al. 2012) facility. High resolution dust continuum map at 350  $\mu\text{m}$  (resolution  $\sim 8''.5$ ; Manuel et al. 2015) observed using the Second-generation Submillimeter High Angular Resolution Camera (SHARC-II) facility. The SHARC-II continuum map was smoothed by a Gaussian function with a width of 3 pixels.

The  $^{13}\text{CO}(J=1-0)$  line data were collected from the FOREST Unbiased Galactic plane Imaging survey with the Nobeyama 45-m telescope (FUGIN; Umemoto et al. 2017) survey. The  $^{13}\text{CO}$  data cube was smoothed with a Gaussian function, yielding a spatial resolution of  $35''$ .

## 3 RESULTS

### 3.1 Physical environment of G25.4NW

In this section, we explore the distribution of the dust, molecular, and ionized emission toward areas of several parsecs around G25.4NW.

#### 3.1.1 *Spitzer* and THOR maps of G25.4NW

Figure 1a displays a three-color composite map made using the *Spitzer* 8.0  $\mu\text{m}$  (in red), 4.5  $\mu\text{m}$  (in green), and 3.6  $\mu\text{m}$  (in blue) images. The radio 1690 MHz continuum contours are also overlaid on the color-composite map, indicating the location of the H II region G25.4NW. The radio continuum map at 1690 MHz is obtained from the THOR survey, which provides six radio continuum maps at 1060, 1310, 1440, 1690, 1820, and 1950 MHz (Bihl et al. 2016). The other five THOR maps also show a similar morphology of the H II region as in the map at 1690 MHz (not presented here). The excess 4.5  $\mu\text{m}$  emission is found in the *Spitzer* color composite map, showing the location of the previously reported EGO in the direction of the continuum source J18354S. No radio counterpart is seen toward J18354S in the THOR continuum maps, while the continuum source J18354N is associated with the H II region. We find the H II region G25.4NW in the catalog of THOR radio continuum sources, which is designated as G25.397–0.141 with a positive spectral index ( $\alpha \sim 0.83$ ; Bihl et al. 2016). The radio spectral index is determined using the radio peak fluxes at six THOR bands. The positive  $\alpha$  value suggests the thermal free-free emission from the H II region G25.4NW (e.g., Rybicki & Lightman 1979; Longair 1992).

In each THOR continuum map, we employed the *clumpfind* IDL program (Williams et al. 1994) to estimate the total flux density ( $S_{\nu}$ ) of the H II region G25.4NW, which is used to compute the number of Lyman continuum photons  $N_{\text{UV}}$  of the H II region. The values of  $S_{\nu}$  at 1060, 1310, 1440, 1690, 1820, and 1950 MHz are estimated to be about 2.1,

**Table 1.** List of different surveys studied in this paper.

Survey	Wavelength/Frequency/line(s)	Resolution (″)	Reference
Coordinated Radio and Infrared Survey for High-Mass Star Formation (CORNISH)	5 GHz	~1.5	Hoare et al. (2012)
The HI/OH/Recombination line survey of the inner Milky Way (THOR)	1–2 GHz	~25	Beuther et al. (2016)
FUGIN survey	$^{12}\text{CO}$ , $^{13}\text{CO}$ , $\text{C}^{18}\text{O}$ ( $J = 1-0$ )	~20	Umamoto et al. (2017)
APEX Telescope Large Area Survey of the Galaxy (ATLASGAL)	870 $\mu\text{m}$	~19.2	Schuller et al. (2009)
<i>Herschel</i> Infrared Galactic Plane Survey (Hi-GAL)	70–500 $\mu\text{m}$	~5.8–37	Molinari et al. (2010a)
<i>Spitzer</i> Galactic Legacy Infrared Mid-Plane Survey Extraordinaire (GLIMPSE)	3.6–8.0 $\mu\text{m}$	~2	Benjamin et al. (2003)
UKIDSS near-infrared Galactic Plane Survey (GPS)	1.25–2.2 $\mu\text{m}$	~0.8	Lawrence et al. (2007)
UKIRT Wide-field Infrared Survey for H2 (UWISH2)	2.12 $\mu\text{m}$	~0.8	Froebrich et al. (2011)
UKIRT Wide-field Infrared Survey for Fe+ (UWIFE)	1.64 $\mu\text{m}$	~0.8	Lee et al. (2014)

2.3, 2.5, 2.7, 2.8, and 3.0 Jy, respectively. We adopted the following equation to estimate the value of  $N_{\text{UV}}$  (Matsakis et al. 1976):

$$N_{\text{UV}}(s^{-1}) = 7.5 \times 10^{46} \left( \frac{S_{\nu}}{\text{Jy}} \right) \left( \frac{D}{\text{kpc}} \right)^2 \left( \frac{T_e}{10^4 \text{K}} \right)^{-0.45} \times \left( \frac{\nu}{\text{GHz}} \right)^{0.1} \quad (1)$$

where  $S_{\nu}$  (in Jy) is defined earlier,  $D$  is the distance in kpc,  $T_e$  is the electron temperature, and  $\nu$  is the frequency in GHz. In this calculation, we considered an electron temperature of 10000 K and  $D = 5.7$  kpc. The values of  $\log N_{\text{UV}}$  of the H II region at 1060, 1310, 1440, 1690, 1820, and 1950 MHz are determined to be about 48.7, 48.8, 48.8, 48.8, 48.9, and  $48.9 s^{-1}$ , respectively. It implies that the derived value of  $\log N_{\text{UV}}$  is similar in each THOR band. Following the work of Panagia (1973), we find that the H II region G25.4NW is excited by an O6–O7 class star, which is in agreement with the earlier published results (Zhu et al. 2011; Ai et al. 2013).

### 3.1.2 *Herschel*, ATLASGAL, and FUGIN maps of G25.4NW

In Figure 1b, we show the integrated  $^{13}\text{CO}$  intensity map at [89.5, 101.2]  $\text{km s}^{-1}$  superimposed with the ATLASGAL 870  $\mu\text{m}$  continuum contours. The FUGIN  $^{13}\text{CO}$  intensity map shows a molecular condensation hosting the dust continuum sources J18354N and J18354S. Note that the resolution of the FUGIN line data is insufficient to reveal inner molecular structures of these two distinct continuum sources. Using the ATLASGAL 870  $\mu\text{m}$  continuum data, Urquhart et al. (2018) reported the total flux densities (dust temperature ( $T_d$ )) of J18354N and J18354S to be  $\sim 36.7$  Jy (34.4 K) and  $\sim 26.6$  Jy (24.8 K), respectively (see also Urquhart et al. 2014). However, they computed the masses of both the continuum sources at a far-side distance of 10.2 kpc. But, the near-side distance of the sources has been preferred in the literature (Zhu et al. 2011; Ai et al. 2013; Zhang et al. 2019, 2020). Therefore, using these observed parameters and  $D = 5.7$  kpc, we compute the masses of J18354N and J18354S to be  $\sim 3150 M_{\odot}$  and  $\sim 3515 M_{\odot}$ , respectively. Urquhart et al. (2014) reported the semi-major and semi-minor axes of the ellipse bounding the clump J18354N, which are  $26''$  ( $\sim 0.72$  pc) and  $21''$  ( $\sim 0.58$  pc), respectively. In the case of the clump J18354S, the semi-major and semi-minor axes are  $21''$  ( $\sim 0.58$  pc) and  $18''$  ( $\sim 0.50$  pc), respectively.

The calculation utilized the following equation (Hildebrand 1983) to compute the mass of each continuum source

(see also equation 1 in Dewangan et al. 2016):

$$M = \frac{D^2 F_{\nu} R_t}{B_{\nu}(T_D) \kappa_{\nu}} \quad (2)$$

where  $F_{\nu}$  is the total integrated flux (in Jy),  $D$  is the distance (in kpc),  $R_t$  is the gas-to-dust mass ratio,  $B_{\nu}$  is the Planck function for a dust temperature  $T_D$ , and  $\kappa_{\nu}$  is the dust absorption coefficient. In this calculation, we considered  $\kappa_{\nu} = 1.85 \text{ cm}^2 \text{ g}^{-1}$  at 870  $\mu\text{m}$  (Schuller et al. 2009),  $R_t = 100$ , and  $D = 5.7$  kpc.

In Figure 1b, the positions of the infrared-excess sources/YSOs (from Dewangan et al. 2015) are also marked by circles. Due to saturation of the *Spitzer* 24  $\mu\text{m}$  image of G25.4NW, Dewangan et al. (2015) employed the *Spitzer* 3.6–8.0  $\mu\text{m}$  and the UKIDSS GPS HK photometric data to identify these YSOs. About a dozen of YSOs are distributed toward the molecular condensation. However, no intense star formation activity or clustering of YSOs is seen toward both the continuum sources J18354N and J18354S. But, the MSF activity is found toward both the continuum sources.

Figure 1c displays a three-color composite map made using the *Herschel* 250  $\mu\text{m}$  (in red), 160  $\mu\text{m}$  (in green), and 70  $\mu\text{m}$  (in blue) images. The continuum sources J18354N and J18354S are clearly evident in the *Herschel* color composite map. Additionally, we also notice the existence of parsec scale filaments toward J18354N. Figure 2a displays the *Herschel* temperature ( $T_d$ ) map, depicting the warm dust emission ( $T_d \sim 23$ –39 K) toward the H II region G25.4NW. On the other hand, the source J18354S is seen with  $T_d$  of  $\sim 22$ –23.2 K.

### 3.1.3 New candidate hub-filament system in G25.4NW

In Figure 1c, we find a hint of the presence of embedded filaments. In order to further explore the embedded filaments, we processed the *Herschel* 160  $\mu\text{m}$  image through an edge detection algorithm (i.e. Difference of Gaussian (DoG); see Gonzalez & Woods 2011; Assirati et al. 2014; Dewangan et al. 2017b, 2020). In Figure 2b, we display a two color-composite map made using the *Herschel* 160  $\mu\text{m}$  image and the DoG processed 160  $\mu\text{m}$  image. The color-composite map is also overlaid with the ATLASGAL 870  $\mu\text{m}$  continuum contours, and enables us to visually examine embedded filaments in the direction of G25.4NW or J18354N, which are indicated by solid curves. Based on the observed configuration of the filaments, we find the existence of a “hub-filament” system in G25.4NW (e.g., Myers 2009; Schneider et al. 2012; Baug et al. 2015; Dewangan et al. 2015, 2018, 2020).

To further explore a hub-filament system in G25.4NW, the SHARC-II 350  $\mu\text{m}$  continuum map and contours are presented in Figure 2c. We also mark the peak positions of the dust clumps traced in the ATLASGAL 870  $\mu\text{m}$  map (see multiplication symbols in Figure 2c). The SHARC-II sub-mm image has higher spatial resolution than the *Herschel* sub-mm images at 160–500  $\mu\text{m}$ , allowing us to gain further insight into the spatial morphology of each dust clump. Using the SHARC-II sub-mm image, a zoomed-in view of an area around G25.4NW is presented in Figure 3a. The H II region G25.4NW or J18354N is exclusively traced at the central hub, and five parsec scale filaments seem to be converging on this hub. By eye examination of the SHARC-II image reveals the compact hub with low aspect ratio (length/diameter) and filaments with high aspect ratio. None of these filaments appear to be spatially connected with the continuum source J18354S (see contours in Figure 2c). However, both the continuum sources are well located within the outer contours of the 350 and 870  $\mu\text{m}$  continuum emission and the molecular condensation (extent  $\sim 3.7$  pc; see Figures 1 and 2). Note that the hub-filament system is not resolved in the ATLASGAL 870  $\mu\text{m}$  continuum map and the FUGIN  $^{13}\text{CO}$  data (see Figure 1b). Hence, new molecular line observations with a higher resolution (below 10'') will be helpful to explore the gas motions toward the hub-filament system.

Overall, we investigate a new candidate hub-filament system in H II region G25.4NW, which is not yet reported in the literature (e.g., Zhu et al. 2011; Ai et al. 2013; Kumar et al. 2020).

### 3.1.4 Ionized clumps in the hub

In the direction of the central hub, high resolution CORNISH radio 5 GHz continuum emission contours are presented in Figure 3b. At least four emission peaks are detected in the 5 GHz continuum map. With the application of the *clumpfind* program in the 5 GHz continuum map, we computed the total flux of the H II region G25.4NW (deconvolved effective radii ( $R_{\text{HII}}$ )) to be  $\sim 2$  Jy ( $\sim 0.2$  pc). Using the equation 1, this flux density yields the value of  $\log N_{\text{UV}}$  to be 48.8, which corresponds to a powering star of spectral type O7–O6.5. This outcome is consistent with the analysis of the THOR radio continuum data (see Section 3.1.1).

The *clumpfind* algorithm also reveals four ionized clumps in the CORNISH map, which are designated as Ia, Ib, Ic, and Id. The boundary of each ionized clump is also presented in Figure 3b. The flux densities (deconvolved angular sizes) of the ionized clumps Ia, Ib, Ic, and Id are about 1408 mJy ( $4''.5 \times 6''.5$ ), 387 mJy ( $4'' \times 6''$ ), 73 mJy ( $3'' \times 2''.4$ ), and 106 mJy ( $2''.6 \times 4''.1$ ), respectively. The deconvolved effective radii ( $R_{\text{HII}}$ ) of the ionized clumps Ia, Ib, Ic, and Id are about 0.15, 0.11, 0.06, and 0.07 pc, respectively. Using the equation 1, we determine  $\log N_{\text{UV}}$  of Ia, Ib, Ic, and Id to be 48.6, 48.0, 47.3, and 47.5  $\text{s}^{-1}$ , respectively. In this calculation, we utilized  $T_e = 10000$  K and  $D = 5.7$  kpc. Following the work of Panagia (1973), we find that the ionized clumps Ia, Ib, Ic, and Id are excited by O8V, B0–O9.5V, B0.5–B0V, and B0.5–B0V type stars, respectively. Therefore, the CORNISH continuum map favours the presence of multiple massive stars (including an O-type star) in the central hub.

## 3.2 Multi-wavelength high-resolution images of the central hub

In the direction of G25.4NW, different wavelengths are examined to explore the central hub. Figures 4a–4e show images at UWIFE 1.64  $\mu\text{m}$  [Fe II] (with continuum), UKIDSS GPS 2.2  $\mu\text{m}$  K-band, UWISH2 2.12  $\mu\text{m}$  H<sub>2</sub> (with continuum), *Spitzer* 8.0  $\mu\text{m}$ , SOFIA/FORCAST 19.7  $\mu\text{m}$ , respectively. The peak position of the source J18354N traced in the ATLASGAL 870  $\mu\text{m}$  map is marked by a multiplication symbol. In the K-band and H<sub>2</sub> images, we find a compact NIR feature (extent  $\sim 0.2$  pc), which is outlined by a solid curve in Figures 4a–4e (see also Figure 3 in Zhu et al. 2011). The images at 8.0  $\mu\text{m}$  and 19.7  $\mu\text{m}$  are known to trace the warm dust emission. In Figure 4f, the CORNISH radio 5 GHz continuum contours are overlaid on the H<sub>2</sub> image. The compact NIR feature is seen in the direction of the ionized clump Ia. Furthermore, the peak emission in the 8.0 and 19.7  $\mu\text{m}$  continuum images is found toward the compact NIR feature, where at least three K-band objects are seen. Among these K-band sources, only one object appears to be detected in the 1.64  $\mu\text{m}$  [Fe II] image, indicating the existence of embedded K-band sources. This argument is supported by the fact that one can easily trace embedded sources in the longer wavelength images ( $> 2$   $\mu\text{m}$ ), where lower dust extinction is expected.

Using the ALMA continuum emission at 1.3 mm (beam size  $\sim 0''.82 \times 0''.58$  or 4675 AU  $\times$  3305 AU), a zoomed-in view of G25.4NW is presented in Figure 5a (see a solid box in Figure 4e). At least four prominent continuum peaks (i.e., c1, c2, c3, and c4) are indicated in Figure 5a. In order to identify cores, the *clumpfind* program was employed in the 1.3 mm continuum map. At least four compact continuum sources (i.e., c1–c4) are depicted toward G25.4NW, and the boundary of each continuum source is displayed in Figure 5b. The total flux densities (deconvolved angular sizes) of the continuum sources c1, c2, c3, and c4 are obtained to be about 366 mJy ( $2''.4 \times 4''.7$ ), 237 mJy ( $1''.8 \times 3''.1$ ), 220 mJy ( $2''.8 \times 2''.5$ ), and 195 mJy ( $3''.1 \times 2''.9$ ), respectively. Using the equation 2, the masses of the continuum sources c1, c2, c3, and c4 are computed to be  $\sim 130$ ,  $\sim 85$ ,  $\sim 80$ , and 70  $M_{\odot}$ , respectively. In this estimation, we considered  $\kappa_{\nu} = 0.9 \text{ cm}^2 \text{ g}^{-1}$  at 1.3 mm (Ossenkopf & Henning 1994),  $T_D = 34.5$  K (see Section 3.1), and  $D = 5.7$  kpc. Based on the *Herschel* temperature map and the previously reported  $T_d$ , in this paper, we choose the value of  $T_d \sim 34.5$  K as the representative value of J18354N. Using the sub-mm/mm continuum maps, the uncertainty in the mass calculation could be typically  $\sim 20\%$  and at largest  $\sim 50\%$ , which is mainly contributed by various uncertainties in the assumed dust temperature, opacity, and measured flux.

A comparison of the ALMA 1.3 mm continuum emission with the continuum images at *Spitzer* 8.0  $\mu\text{m}$  and CORNISH 5 GHz is presented in Figures 6a and 6b, respectively. The 1.3 mm continuum peaks (i.e., c1, c2, and c3) are found toward the ionized clump Ia, where the warm dust emission is traced in the MIR images. Additionally, the remaining peak c4 is also seen toward the CORNISH ionized clump Ib.

In the direction of the compact NIR feature, Figure 6c presents the 1.3 mm continuum emission contours overlaid on the H<sub>2</sub> image. An elongated feature (extent  $\sim 0.2$  pc) containing three continuum peaks (i.e., c1, c2, and c3) is

evident in the 1.3 mm continuum map. The separation between peaks c1 and c2 is about 7260 AU, while the separation between peaks c2 and c3 is about 13390 AU. We do not find the positions of any point-like sources exactly coincident with the continuum peaks (see arrows in Figure 6c). However, the central continuum peak, c2 is seen very close to one K-band source that is not detected in the [Fe II] image.

#### 4 DISCUSSION

The present paper employs several sub-mm maps of the H II region G25.4NW associated with the dust continuum source J18354N (mass  $\sim 3150 M_{\odot}$ ; see Section 3.1). For the first time, we report a new picture in G25.4NW, which is a hub-filament configuration (see Section 3.1.3). Morphologically this system consists of five parsec scale filaments, which are directed to the central hub (see Figure 3a). High resolution continuum maps observed in the NIR, mm, and radio wavelengths (resolution  $\sim 0''.6-1''.5$ ) have enabled us to uncover hidden substructures in the central hub. The presence of at least four ionized clumps (Ia–Id) excited by massive OB stars is investigated toward the central hub (see Figure 3b). The ALMA 1.3 mm continuum map detects three continuum sources c1–c3 (mass  $\sim 80-130 M_{\odot}$ ) and one source c4 (mass  $\sim 70 M_{\odot}$ ) toward the ionized clumps Ia and Ib, respectively. The continuum sources c1–c3 are well distributed within an elongated feature (extent  $\sim 0.2$  pc) depicted in the ALMA 1.3 mm continuum map. This particular feature spatially coincides with the ionized clump Ia powered by a single O8V-type star, and is seen close to the compact NIR feature (extent  $\sim 0.2$  pc) containing embedded objects (see Figure 6). Sub-arcsecond radio continuum observations will be helpful for further resolving the ionized clump Ia.

It appears that there are no massive prestellar cores in J18354N. These observed substructures are exclusively found toward the central hub or at the center of the massive clump J18354N, and seem to be most closely associated with MSF. It may also be inferred with the detection of the warm dust emission ( $T_d \sim 23-39$  K) toward the source J18354N, suggesting that the clump J18354N is heated internally by stellar feedback from massive stars (i.e., ionized emission, stellar wind, and radiation pressure). Collectively, the existence of a small cluster of massive stars is evident in the central hub of the hub-filament system in G25.4NW.

Recently, Zhang et al. (2020) analyzed the  $\text{NH}_3$  line data (beam size  $\sim 4''.1 \times 3''.4$ ) toward the continuum source J18354S or G25.38 (mass  $\sim 3515 M_{\odot}$ ). However, these authors do not include an area around the source J18354N. In order to study the  $\text{NH}_3$  emission toward the source J18354N, we examined this publicly available  $\text{NH}_3$  (1,1) data cube, which covers an area containing J18354N and J18354S (not shown here). However, no  $\text{NH}_3$  (1,1) emission is detected toward J18354N. This particular exercise and the observed 350  $\mu\text{m}$  dust continuum emission show that the candidate hub-filament system J18354N is not a piece of the continuum source J18354S. As mentioned earlier, both the continuum sources are located within common ATLASGAL 870  $\mu\text{m}$  contour (see Figure 2b). It is likely that the stellar feedback from massive stars in G25.4NW may influence the environment of J18354S/G25.38. In this context, the knowledge of various pressure components (e.g., pressure of an H II region

( $P_{\text{HII}}$ ), radiation pressure ( $P_{\text{rad}}$ ), and stellar wind ram pressure ( $P_{\text{wind}}$ ) driven by OB-type stars (see Dewangan et al. 2015, 2017a, for more details) will be helpful to study the feedback of massive stars. However, such study is beyond the scope of this paper.

To explain the formation of massive stars, two groups of theoretical scenarios have been reported in the literature, which are “core-fed” and “clump-fed”. In the “core-fed” group, turbulent core accretion model explains the birth of a massive star (or a binary or a small number of multiples) via the collapse of a massive, isolated, and gravitationally bound prestellar core (McKee & Ostriker 2003). The competitive accretion and global hierarchical collapse (GHC) scenarios are part of the “clump-fed” group (see a review article by Rosen et al. 2020, for more details). The competitive accretion model predicts a mass accumulation through global gravitational forces in the central region of the clumps enclosed by smaller scale multiple cores (Bonnell et al. 2002, 2004; Bonnell & Bate 2006). According to this model, the location of more massive stars is expected at the centre of a protostellar cluster. In the GHC model, one can expect gravitationally driven fragmentation in star-forming molecular clouds, and one can also expect large scale accretion flows to directly feed the sites of massive stars (see Vázquez-Semadeni et al. 2009, 2017, 2019; Smith et al. 2009). In other words, the model predicts the fast growth of cores through accretion streams linked with the GHC of clouds (e.g., Smith et al. 2009).

As highlighted in Section 1, the presence of a hub-filament configuration hints the onset of the global non-isotropic collapse scenario (GNIC; Motte et al. 2018; Tigé et al. 2017, and see also Section 1), which includes the basic ingredients of the GHC and clump-fed accretion models. Ultimately the global non-isotropic collapse scenario suggests that an infrared-bright massive protostar forms via the inflow from larger scales, and produces an H II region (in a time of few  $10^5-10^6$  yr) through its stellar UV radiation. Some known sites hosting a hub-filament system are Ophiuchus (Myers 2009), Taurus (Myers 2009), Rosette (Schneider et al. 2012), IRDC G14.225–0.506 (Busquet et al. 2013), SDC335.579–0.292 (Peretto et al. 2013), Sh 2-138 (Baug et al. 2015), W42 (Dewangan et al. 2015), IRAS 05480+2545 (Dewangan et al. 2017b), Sh 2-53 (Baug et al. 2018), and Monoceros R2 (Treviño-Morales et al. 2019), and G18.88–0.49 (Dewangan et al. 2020). More details of the global non-isotropic collapse scenario can be found in Tigé et al. (2017); Motte et al. (2018) (see also Treviño-Morales et al. 2019; Dewangan et al. 2020).

As mentioned in this section, in G25.4NW, the central hub hosts infrared-bright massive stars and multiple cores, and are surrounded by filaments. Hence, the GNIC scenario appears to explain the observed morphology and MSF in the continuum source J18354N. The observed results may correspond to the infrared-bright protostellar core phase (see step 5 in Tigé et al. 2017). However, the applicability of the turbulent core accretion model is unlikely in G25.4NW. This paper does not present the gas motion toward the candidate hub-filament system in G25.4NW. Hence, to give a conclusive interpretation concerning the target G25.4NW, high resolution molecular line observations will be helpful to trace the signatures of the gas flow along the filaments to the central hub and interactions among cores.

## 5 SUMMARY AND CONCLUSIONS

This paper focuses on the understanding of the process of mass accumulation in MSF. In this context, we present multi-scale and multi-wavelength data (including ALMA continuum maps) of the Galactic H II region G25.4NW, which is situated at a near-side distance of 5.7 kpc. The main findings are:

- In G25.4NW, the *Herschel* sub-mm 160 and 250  $\mu\text{m}$  continuum images (resolution  $\sim 12\text{--}18''$ ) and the SHARC-II 350  $\mu\text{m}$  continuum map (resolution  $\sim 8''.5$ ) show a new candidate hub-filament system containing five parsec scale filaments and a central compact hub.
- The H II region G25.4NW with previously known thermal spectral index is traced toward the central hub, and is associated with the warm dust emission (at  $T_d \sim 23\text{--}39$  K) inferred from the *Herschel* temperature map (resolution  $\sim 12''$ ).
- In the direction of the H II region G25.4NW, high resolution 5 GHz radio continuum map (resolution  $\sim 1''.5$ ) reveals four ionized clumps (i.e., Ia, Ib, Ic, and Id), which are powered by massive OB-type stars.
- A compact NIR feature (extent  $\sim 0.2$  pc) containing three K-band stars is investigated toward the ionized clump Ia (deconvolved size  $\sim 0.12 \times 0.18$  pc), which is excited by an O8V-type star.
- In the direction of the ionized clump Ia, high resolution ALMA 1.3 mm continuum map (resolution  $\sim 0''.82 \times 0''.58$ ) reveals an elongated feature (extent  $\sim 0.2$  pc) hosting three continuum sources (mass  $\sim 80\text{--}130 M_\odot$ ). These 1.3 mm continuum sources are found close to the compact NIR feature, where multiple massive stars are being formed.

Overall, our observational outcomes show the existence of a cluster of massive stars in the central hub. Hence, we suggest the onset of the GNIC scenario in G25.4NW, which successfully explains the birth of massive stars.

## ACKNOWLEDGMENTS

We are grateful to the anonymous reviewer for the constructive comments and suggestions, which greatly improved the scientific contents of the paper. The research work at Physical Research Laboratory is funded by the Department of Space, Government of India. This work is based [in part] on observations made with the *Spitzer* Space Telescope, which is operated by the Jet Propulsion Laboratory, California Institute of Technology under a contract with NASA. This publication makes use of data from FUGIN, FOREST Unbiased Galactic plane Imaging survey with the Nobeyama 45-m telescope, a legacy project in the Nobeyama 45-m radio telescope. This paper makes use of the following ALMA archive data: ADS/JAO.ALMA#2017.1.01116.S. ALMA is a partnership of ESO (representing its member states), NSF (USA) and NINS (Japan), together with NRC (Canada), MOST and ASIAA (Taiwan), and KASI (Republic of Korea), in cooperation with the Republic of Chile. The Joint ALMA Observatory is operated by ESO, AUI/NRAO and NAOJ.

## Data availability

The CORNISH 5 GHz radio continuum data underlying this article are available from the publicly accessible CORNISH image cutout server<sup>1</sup>. The THOR radio continuum data underlying this article are available from the publicly accessible THOR website<sup>2</sup>. The ALMA continuum data underlying this article are available from the publicly accessible JVO ALMA FITS archive<sup>3</sup>. The FUGIN molecular line data underlying this article are available from the publicly accessible website<sup>4</sup>. The ATLASGAL 870  $\mu\text{m}$  continuum data underlying this article are available from the publicly accessible ATLASGAL database server<sup>5</sup>. The *Herschel*, *Spitzer*, SOFIA, SHARK-II continuum data underlying this article are available from the publicly accessible NASA/IPAC infrared science archive<sup>6</sup>. The *Herschel* temperature map underlying this article is available from the publicly accessible website<sup>7</sup>. The UKIDSS GPS data underlying this article are available from the publicly accessible website<sup>8</sup>. The H<sub>2</sub> data underlying this article are available from the publicly accessible website<sup>9</sup>. The Fe [II] data underlying this article are available from the publicly accessible website<sup>10</sup>.

## REFERENCES

- Ai M., Zhu M., Xiao Li, Su H.-Q., 2013, RAA, 13, 935  
 Assirati L., Silva N. R., Berton L., Lopes A. A., Bruno O. M., 2014, Journal of Physics: Conference Series, 490(1), 2014  
 Baug T., Ojha D. K., Dewangan L. K., Ninan J. P., Bhatt B. C., Ghosh S. K., Mallick K. K., 2015, MNRAS, 454, 4335  
 Baug T. et al., 2018, ApJ, 852, 119  
 Benjamin R. A. et al., 2003, PASP, 115, 953  
 Beuther H. et al., 2016, A&A, 595, 32  
 Bihl S. et al., 2016, A&A, 588, 97  
 Bonnell I. A., Bate M. R., 2006, MNRAS, 370, 488  
 Bonnell I. A., Vine S. G., Bate M. R., 2004, MNRAS, 349, 735  
 Bonnell I. A., Bate M. R., Clarke C. J., Pringle J. E., 2002, MNRAS, 323, 785  
 Busquet G. et al., 2013, ApJ, 764, 26  
 Carolan P. B. et al., 2009, MNRAS, 400, 78  
 Dewangan L. K., Luna A., Ojha D. K., Anandarao B. G., Mallick K. K., Mayya Y. D., 2015, ApJ, 811, 79  
 Dewangan L. K., Ojha D. K., Luna A., Anandarao B. G., Ninan J. P., Mallick K. K., Mayya Y. D., 2016, ApJ, 819, 66  
 Dewangan L. K., Ojha D. K., Zinchenko I., Janardhan P., Luna, A., 2017a, ApJ, 834, 22

<sup>1</sup> [https://cornish.leeds.ac.uk/public/img\\_server.php/](https://cornish.leeds.ac.uk/public/img_server.php/)

<sup>2</sup> <https://www2.mpia-hd.mpg.de/thor/Overview.html/>

<sup>3</sup> <http://jvo.nao.ac.jp/portal/alma/archive.do/>

<sup>4</sup> <https://nro-fugin.github.io/release/>

<sup>5</sup> <https://www3.mpifr-bonn.mpg.de/div/atlasgal/>

<sup>6</sup> <https://irsa.ipac.caltech.edu/frontpage/>

<sup>7</sup> <http://www.astro.cardiff.ac.uk/research/ViaLactea/>

<sup>8</sup> <http://wsa.roe.ac.uk/>

<sup>9</sup> <http://astro.kent.ac.uk/uwish2/>

<sup>10</sup> <http://gems0.kasi.re.kr/uwifw/>

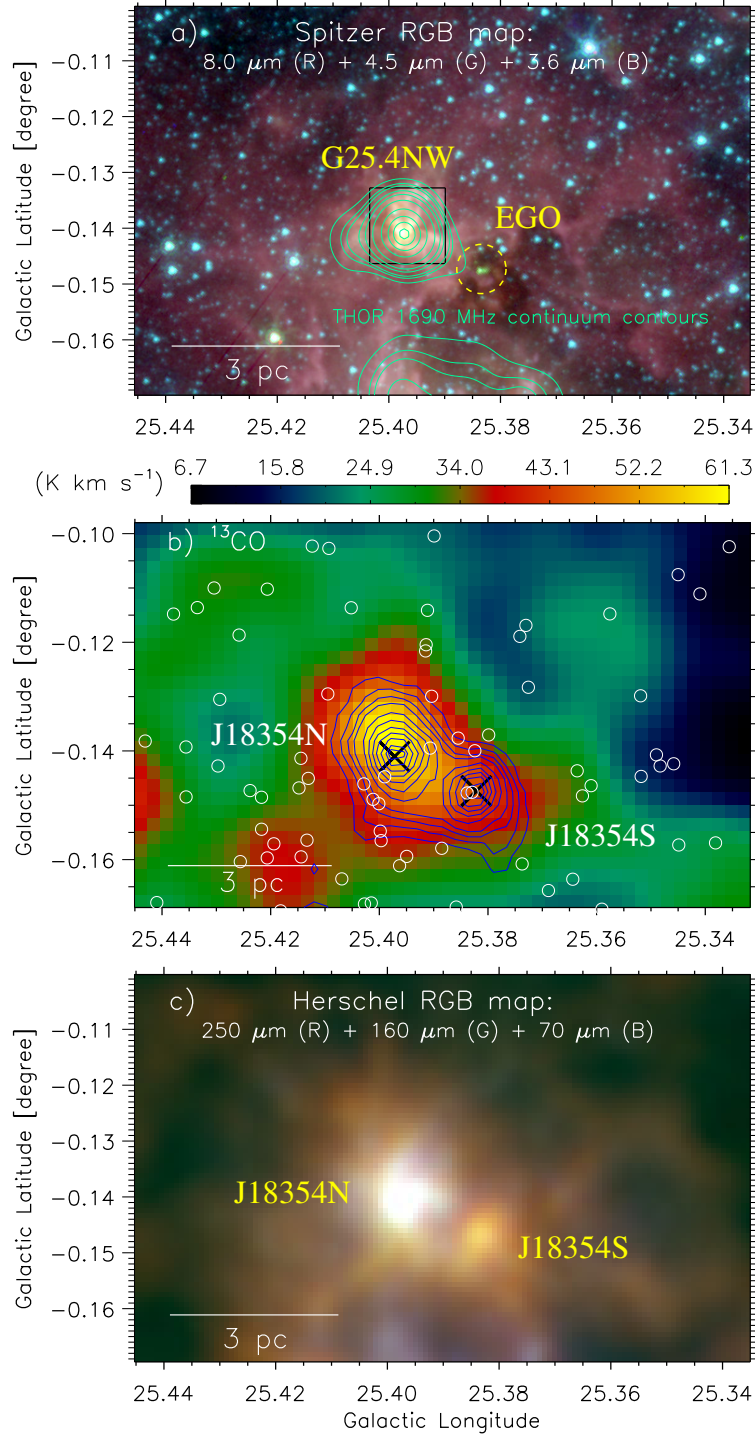


**Figure 1.** a) Overlay of the THOR 1690 MHz radio continuum contours on the *Spitzer* color-composite image of G25.4-0.14 or G25.4NW (area  $\sim 6'.6 \times 4'.2$ ; central coordinates:  $l = 25^\circ.39$ ;  $b = -0^\circ.135$ ) made using 8.0  $\mu\text{m}$  image (red), 4.5  $\mu\text{m}$  image (green), and 3.6  $\mu\text{m}$  image. The black box indicates an area shown in Figures 4a–4f. The radio continuum contours are plotted with the levels of  $(0.05, 0.08, 0.1, 0.15, 0.2, 0.3, 0.5, 0.7, 0.85, 0.97) \times 1.83 \text{ Jy beam}^{-1}$ . An EGO is highlighted by a dashed circle in the figure (see also Figure 4 in Zhu et al. 2011). b) The FUGIN intensity map of the  $^{13}\text{CO}(J=1-0)$  emission integrated over a velocity range of  $[89.5, 101.2] \text{ km s}^{-1}$ . The molecular map is overlaid with the contours of the ATLASGAL 870  $\mu\text{m}$  continuum emission and the positions of the infrared-excess sources (see circles; from Dewangan et al. 2015). The dust continuum contours (in blue) are shown with the levels of  $(0.15, 0.2, 0.25, 0.3, 0.4, 0.5, 0.6, 0.7, 0.8, 0.9, 0.95) \times 4.37 \text{ Jy beam}^{-1}$ . Multiplication symbols show the peak positions of the ATLASGAL dust clumps. c) The *Herschel* color-composite image of G25.4NW made using 250  $\mu\text{m}$  image (red), 160  $\mu\text{m}$  image (green), and 70  $\mu\text{m}$  image. In each panel, the scale bar referring to 3 pc (at a distance of 5.7 kpc) is shown.

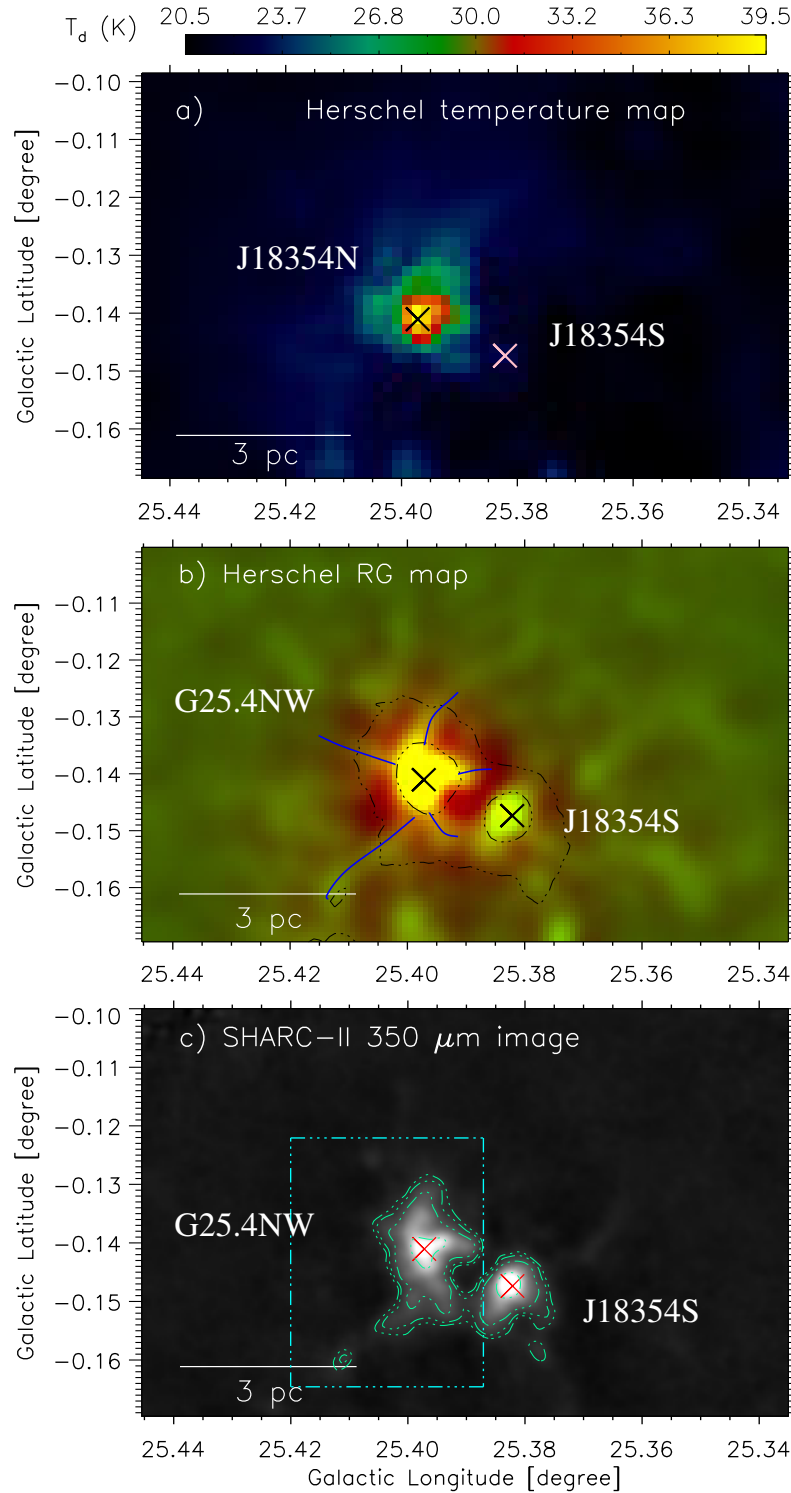


**Figure 2.** a) *Herschel* temperature map of G25.4NW. b) Overlay of the 870  $\mu\text{m}$  continuum contours on a two color-composite map (*Herschel* 160  $\mu\text{m}$  (red) and processed *Herschel* 160  $\mu\text{m}$  (green) images). The *Herschel* 160  $\mu\text{m}$  image is exposed to an “Edge-DoG” algorithm. The 870  $\mu\text{m}$  continuum contours (in black) are also shown with the levels of  $(0.15, 0.5) \times 4.37 \text{ Jy beam}^{-1}$ . Solid curves (in blue) highlight filament-like features in the color-composite map and contours at 350  $\mu\text{m}$ . The contours (in spring green) are plotted with the levels of 1.5, 2.2, 4.1, and 13.6  $\text{Jy beam}^{-1}$ . The continuum image is processed through a Gaussian smoothing function with a width of 3 pixels. The dotted-dashed box (in cyan) indicates an area shown in Figure 3a. In each panel, multiplication symbols show the peak positions of the dust clumps traced in the ATLASGAL 870  $\mu\text{m}$  map (see also Figure 1b).



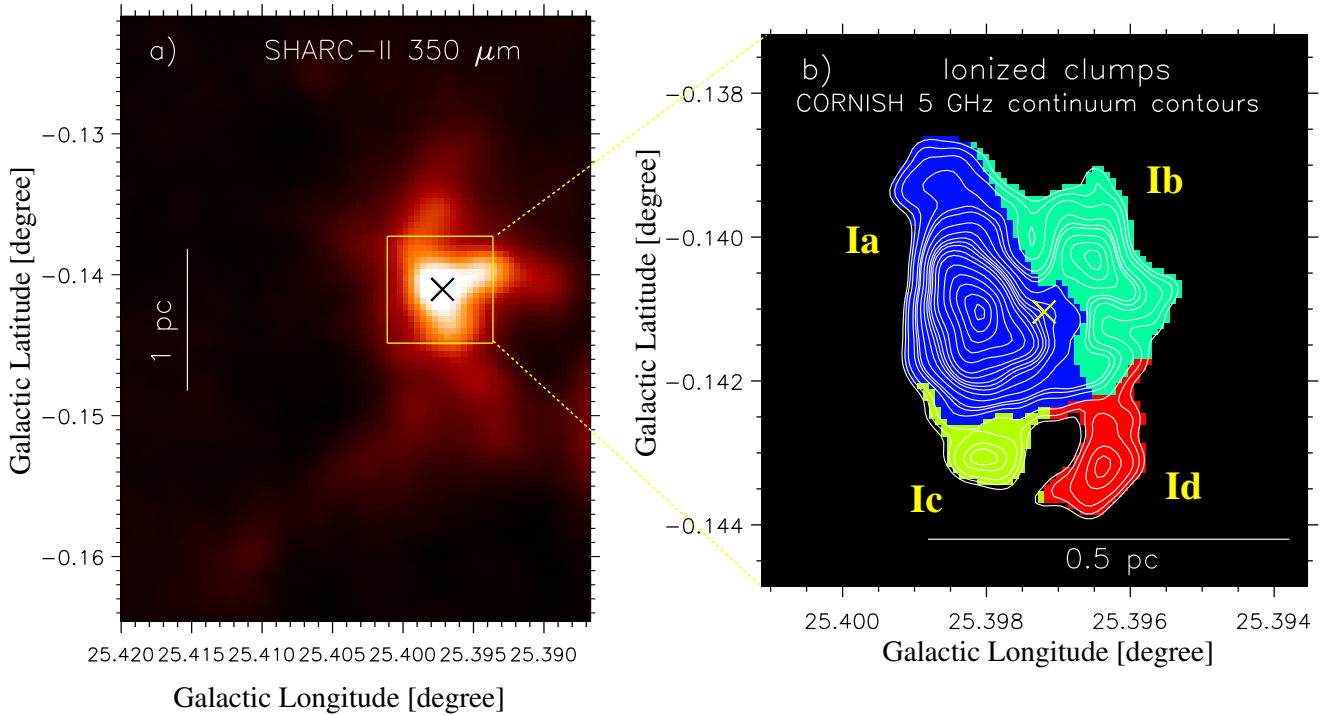


**Figure 3.** a) A zoomed-in view of an area around G25.4NW using the SHARC-II dust continuum image at  $350 \mu\text{m}$  (see a dotted-dashed box in Figure 2c), revealing a candidate hub-filament system. b) The panel displays the CORNISH 5 GHz continuum emission of an area highlighted by a solid box in Figure 3a. The 5 GHz continuum contours (in white) are shown with the levels of (0.058, 0.075, 0.1, 0.15, 0.18, 0.2, 0.25, 0.3, 0.34, 0.37, 0.4, 0.45, 0.5, 0.6, 0.7, 0.8, 0.9, 0.98)  $\times 122.1 \text{ mJy beam}^{-1}$  (where  $1\sigma \sim 0.4 \text{ mJy beam}^{-1}$ ). The background map shows a clumpfind decomposition of the 5 GHz continuum emission, tracing the spatial extension of four ionized clumps (i.e., Ia, Ib, Ic, and Id). In each panel, the multiplication symbol is the same as in Figure 1b.

Dewangan L. K., Ojha D. K., Baug T., 2017b, *ApJ*, 844, 15  
Dewangan L. K., Baug T., Ojha D. K., Ghosh S. K., 2018, *ApJ*, 869, 30  
Dewangan L. K., Ojha D. K., Sharma Saurabh, del Palacio S., Bhadari N. K., Das A., 2020, *ApJ*, 903, 13  
Froeblich D. et al., 2011, *MNRAS*, 413, 480  
Gonzalez R., Woods R., 2011, *Digital Image Processing* (Pearson Education) ISBN 9780133002324  
Herter T. L. et al., 2012, *ApJ*, 749L, 18  
Hildebrand R. H., 1983, *Quarterly Journal of the RAS*, 24, 267  
Hirota T., 2018, *Publication of Korean Astronomical Society*, 33, 21.  
Hoare M. G. et al., 2012, *PASP*, 124, 939  
Kumar M. S. N., Palmeirim P., Arzoumanian D., Inutsuka S. I., 2020, *A&A*, 642, 87  
Lawrence A. et al., 2007, *MNRAS*, 379, 1599  
Lee J. J. et al., 2014, *MNRAS*, 443, 2650  
Lester D. F., Dinerstein H. L., Werner M. W., Harvey P. M., Evans N. J., II, Brown R. L., 1985, *ApJ*, 296, 565  
Liu T., Wu Y., Zhang Q., Ren Z., Guan X., Zhu M., 2011, *ApJ*, 728, 91  
Marsh K. A., Whitworth A. P., Lomax O., 2015, *MNRAS*, 454, 4282  
Marsh K. A. et al., 2017, *MNRAS*, 471, 2730  
Matsakis D. N., Evans N. J., II, Sato T., Zuckerman B., 1976, *AJ*, 81, 172  
McKee C. F., Tan, J. C., 2003, *ApJ*, 585, 850

Merello M., Evans II N. J., Shirley Y. L., Rosolowsky E., Ginsburg A., Bally J., Battersby C., Dunham M. M., 2015, *ApJS*, 218, 1  
Molinari S. et al., 2010a, *A&A*, 518, L100  
Molinari S. et al., 2010b, *PASP*, 122, 314  
Motte F., Bontemps S., Louvet F., 2018, *ARA&A*, 56, 41  
Myers P. C., 2009, *ApJ*, 700, 1609  
Longair M. S., 1992, *High energy astrophysics. Vol.1: Particles, photons and their detection*, 436  
Ossenkopf V., Henning T., 1994, *A&A*, 291, 943  
Panagia N., 1973, *AJ*, 78, 929  
Peretto N. et al., 2013, *A&A*, 555, 112  
Rosen A. L., Offner S. S. R., Sadavoy S. I., Bhandare A., Vázquez-Semadeni E., Ginsburg A., 2020, *SSRv*, 216, 62  
Rybicki G. B., Lightman A. P., 1979, *Radiative processes in astrophysics*  
Schneider N. et al., 2012, *A&A*, 540, L11  
Schuller F. et al., 2009, *A&A*, 504, 415  
Smith R. J., Longmore S., Bonnell I., 2009, *MNRAS*, 400, 1775  
Tigé J. et al. 2017, *A&A*, 602, A77  
Treviño-Morales S. P. et al., 2019, *A&A*, 629, A81  
Tan J. C., Beltrán M. T., Caselli P., Fontani F., Fuente A., Krumholz M. R., McKee C. F., Stolte A., 2014, in *Protostars and Planets VI*, ed. H. Beuther et al. (Tucson, AZ: Univ. Arizona Press), 149  
Umemoto T. et al., 2017 *PASJ*, 69, 78  
Urquhart J. S. et al., 2014, *A&A*, 568, 41  
Urquhart J. S. et al., 2018, *MNRAS*, 437, 1059

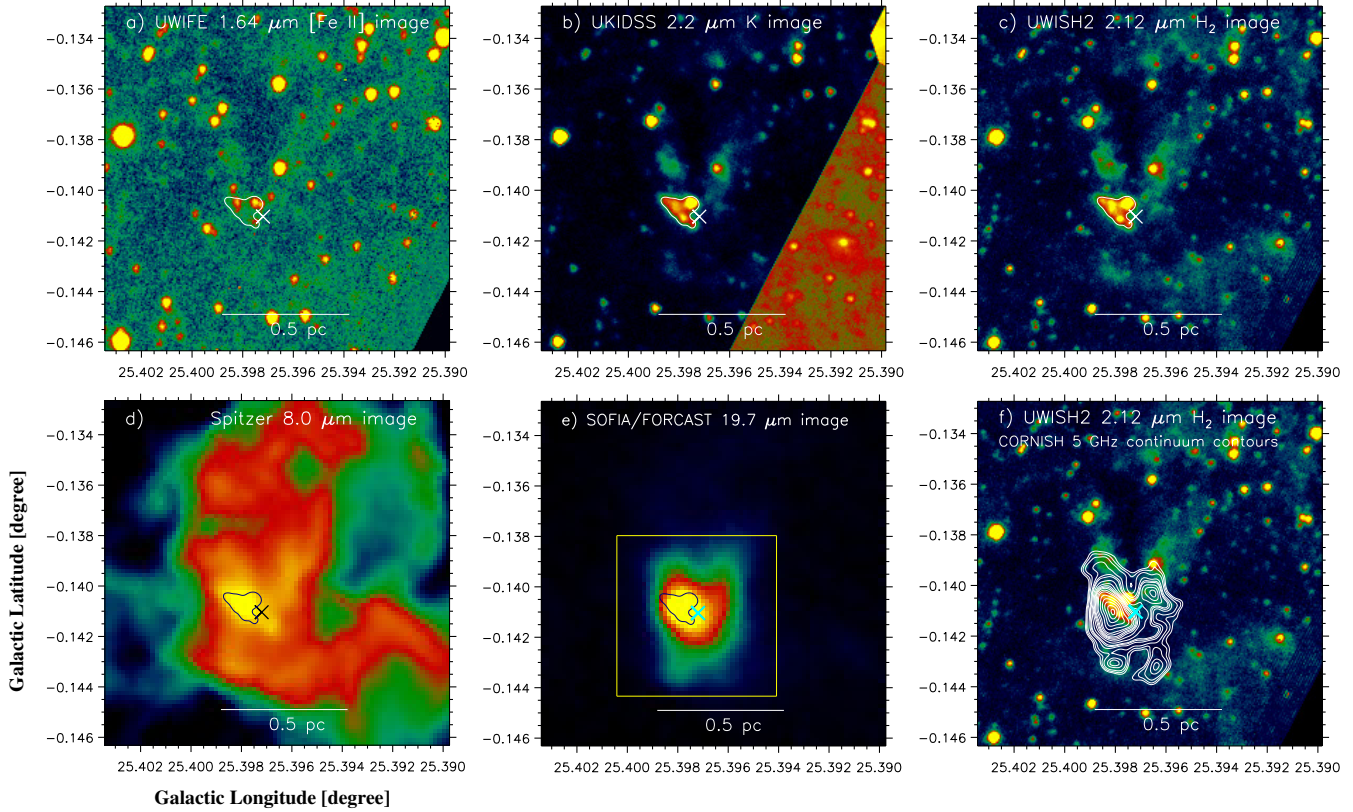


**Figure 4.** Multi-wavelength picture of an area highlighted by a box in Figure 1a. The continuum images are shown at different wavelengths, which are indicated in the panels. A compact NIR feature (extent  $\sim 0.2$  pc) seen in the K-band and H<sub>2</sub> images is indicated by a solid curve in panels “a–e”. In panel “e”, a solid box encompasses the area displayed in Figure 5a. In panel “f”, the CORNISH 5 GHz continuum emission contours are overlaid on the H<sub>2</sub> image, and are the same as in Figure 3b. In all panels, the multiplication symbol is the same as in Figure 3a. In each panel, the scale bar referring to 0.5 pc (at a distance of 5.7 kpc) is displayed.

- Vázquez-Semadeni E., Gómez G. C., Jappsen A. K., Ballesteros-Paredes J., Klessen R. S., 2009, *ApJ*, 707, 1023  
 Vázquez-Semadeni E., González-Samaniego A., Colín P., 2017, *MNRAS*, 467, 1313  
 Vázquez-Semadeni E., Palau A., Ballesteros-Paredes J., Gómez G. C., Zamora-Avilés M., 2019, *MNRAS*, 490, 3061  
 Williams J. P., de Geus E. J., Blitz L., 1994, *ApJ*, 428, 693  
 Wu Y., Zhu M., Wei Y., Xu D., Zhang Q., Fiege J. D., 2005, *ApJ*, 628L, 57  
 Zhang C.-P., Li G.-X., Pillai T., Csengeri T., Wyrowski F., Menten K. M., Pestalozzi M. R., 2020, *A&A*, 638, 105  
 Zhang C.-P. et al., 2019, *A&A*, 627, 85  
 Zhu M., Davis C. J., Wu Y., Whitney B. A., Robitaille T., Peng R., 2020, *ApJ*, 739, 53  
 Zinnecker H., Yorke H. W., 2007, *ARA&A*, 45, 481

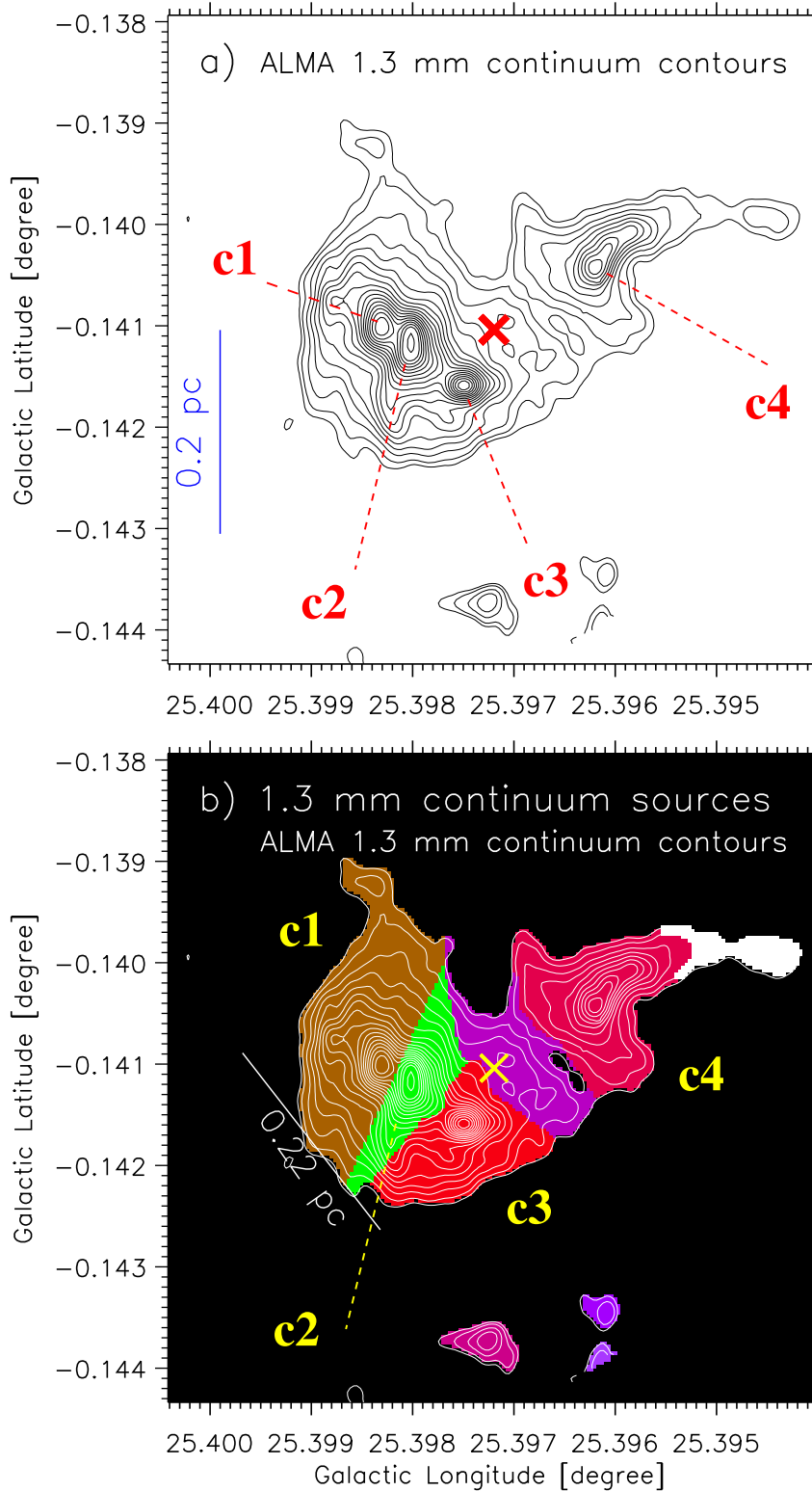


**Figure 5.** a) A zoomed-in view of an area around G25.4NW (see a solid box in Figure 4e). The panel displays the ALMA 1.3 mm continuum emission. The 1.3 mm continuum contours are displayed with the levels of (0.07, 0.1, 0.15, 0.2, 0.25, 0.3, 0.35, 0.4, 0.45, 0.5, 0.55, 0.6, 0.65, 0.7, 0.75, 0.8, 0.85, 0.9, 0.98)  $\times 25.6$  mJy beam $^{-1}$  (where  $1\sigma \sim 0.4$  mJy beam $^{-1}$ ). b) Clumpfind decomposition of the 1.3 mm continuum emission. The panel shows the spatial boundaries of selected continuum sources traced in the 1.3 mm continuum image. The 1.3 mm continuum emission contours are also drawn in the panel (see Figure 5a). In each panel, the multiplication symbol is the same as in Figure 3a.

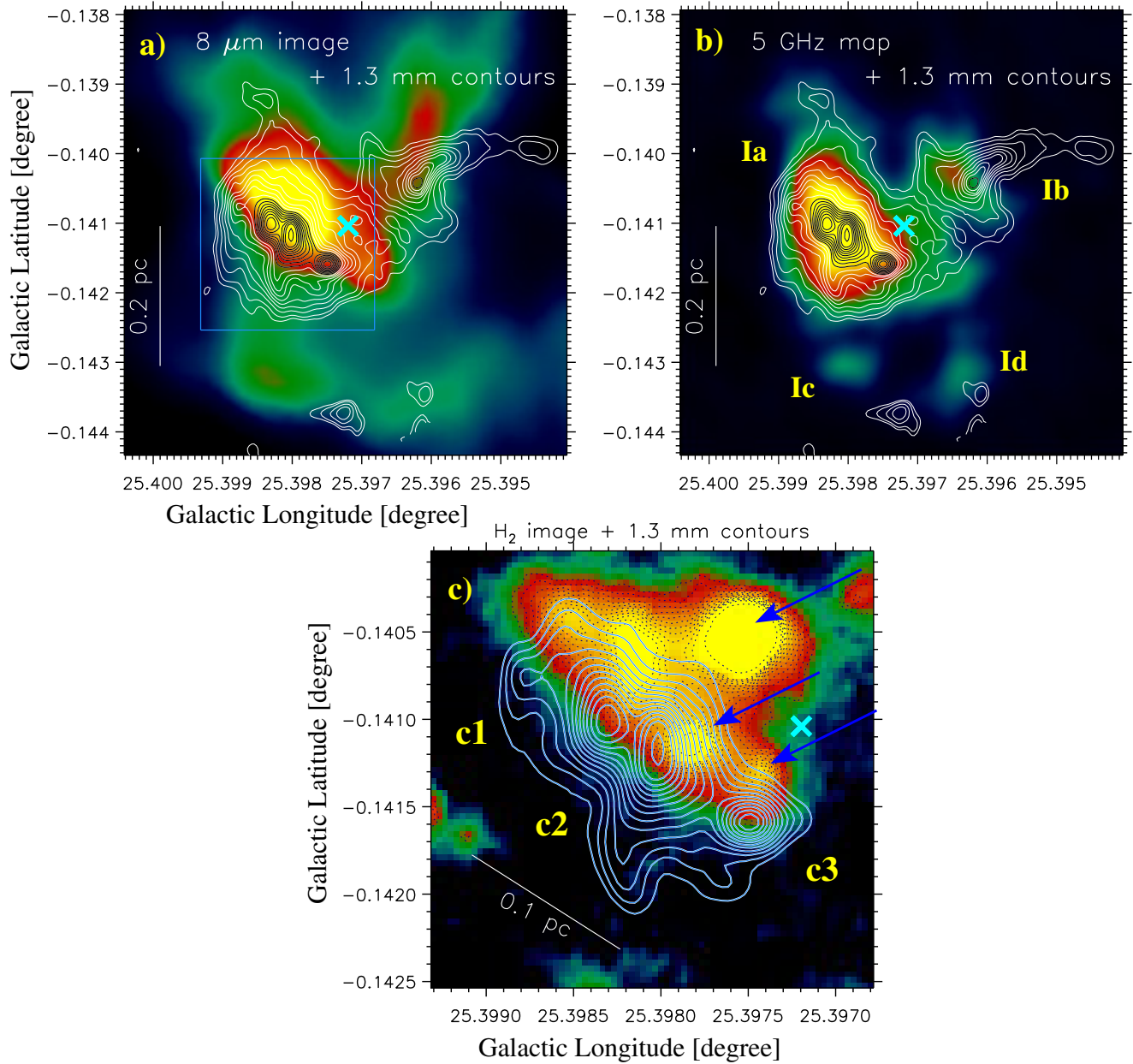


**Figure 6.** a) Overlay of the ALMA 1.3 mm continuum emission contours on a) the *Spitzer* 8.0  $\mu\text{m}$  image, b) the CORNISH 5 GHz continuum map. In panels “a–b”, the contours are the same as in Figure 5a. c) Overlay of the ALMA 1.3 mm continuum emission contours (in dodger blue) on the H<sub>2</sub> image (see a box in Figure 6a). Higher levels of the 1.3 mm continuum contours are shown in the panel (see Figure 5a). The dotted contours (in navy) show the compact NIR feature traced in the H<sub>2</sub> image. Blue arrows highlight the K-band objects. In each panel, the multiplication symbol is the same as in Figure 3a.